The Hall electric field in Earth's magnetotail thin current sheet

San Lu[1], A. V. Artemyev[1,2], V. Angelopoulos[1], Y. Lin[3], X.-J. Zhang[1], J. Liu[1], L. A. Avanov[4], B. L. Giles[4], C. T. Russell[1], R. J. Strangeway[1]

[1]Department of Earth, Planetary, and Space Sciences and Institute of Geophysics and Planetary Physics, University of California, Los Angeles, California, USA

[2]Space Research Institute, RAS, Moscow, Russia

[3]Physics Department, Auburn University, Auburn, Alabama, USA

[4]Heliophysics Science Division, NASA Goddard Space Flight Center, Greenbelt, MD USA

Correspondence to: S. Lu, slu@igpp.ucla.edu

Key Points:

- MMS and THEMIS observations of the Hall electric field in Earth's magnetotail TCS
- The Hall electric field is directed toward the center of the TCS, with an average magnitude of several tenths of 1 mV/m
- Statistics show that the Hall electric field is stronger on the duskside, consistent with predictions from simulations

This article has been accepted for publication and undergone full peer review but has not been through the copyediting, typesetting, pagination and proofreading process which may lead to differences between this version and the Version of Record. Please cite this article as doi: 10.1029/2018JA026202

Abstract

One of the most important properties of Earth's magnetotail thin current sheet (TCS) is that its current is predominantly contributed by magnetized electrons. The Hall electric field, normal to the thin current sheet and generated by charge separation, is critical to the generation of this electron current as well as a dawn-dusk asymmetry of the magnetotail, such as duskside preference of magnetic reconnection and related structures and phenomena. However, systematic investigation of the Hall electric field has so far been lacking. Utilizing observations of TCS by MMS (Magnetospheric Multiscale) and THEMIS (Time History of Events and Macroscale Interactions during Substorm) spacecraft, we study the properties of this field. Our results, from various, complementary methods, show that the Hall electric field E_z (in the Geocentric Solar Magnetospheric, GSM, coordinate system) or E_n (normal to the TCS plane) can be clearly observed to point towards the center of the current sheet. The typical magnitude of this electric field is several tenths of 1 mV/m. Statistics of MMS magnetotail TCS crossings show that the Hall electric field is stronger on the duskside, indicating a stronger Hall effect there, which confirms predictions from global-scale hybrid and particle-in-cell simulations.

1. Introduction

Thin current sheet (TCS) formation in Earth's magnetotail, one of the most important features of the substorm growth phase, occurs before magnetic reconnection releases the stored magnetotail energy, causing charged particle (ion and electron) acceleration and global magnetotail reconfiguration. This magnetotail TCS typically has a strong current density, about 10 $\mathrm{nA/m^2}$, and an ion kinetic scale thickness on the order of several ion Larmor radii or ion inertial lengths (e.g., Petrukovich et al., 2015, and references therein). Although ions

are significantly hotter than electrons in the magnetotail TCS, this strong current density is mainly carried by electrons, as found in both numerical simulations (e.g., Pritchett & Coroniti, 1994; Hesse et al., 1998; Liu et al., 2014) and spacecraft observations (e.g., Runov et al., 2006; Artemyev et al., 2009, 2011; Wang et al., 2018).

In such thin (ion kinetic scale) current sheets, a significant portion of ions becomes demagnetized and cannot convect with magnetic field lines. Electrons, which are lighter and thus mostly magnetized, follow the field lines and move farther towards the neutral plane (TCS center) during TCS thinning driven by external pressure pulses or a cross-tail electric field. This difference between electron and ion response leads to charge separation (the Hall effect, see, e.g., Sonnerup 1979; Nagai et al., 2001; Fu et al., 2006; Lu et al., 2010) and a Hall electric field pointing towards the center of the thin current sheet from both sides (see, e.g., Wygant et al. 2005; Aunai et al., 2011; Korovinskiy et al., 2011; Schindler et al., 2012; Vasko et al. 2014; and references therein). In the presence of this Hall electric field, magnetized particles (ions and electrons) can $\mathbf{E} \times \mathbf{B}$ drift dawnward. The magnetized ions $\mathbf{E} \times \mathbf{B}$ drift dawnward, reducing the total duskward ion current, which is dominated by the ion pressure gradient drift and transient ion motion (see, e.g., discussions in Artemyev & Zelenyi, 2013; Sitnov & Merkin, 2016; and references therein). Electrons are much lighter than ions, so almost all the electrons $\mathbf{E} \times \mathbf{B}$ drift dawnward (e.g., Birn et al., 2004, Zelenyi et al., 2011), which significantly increases the electron contribution to the duskward current. Another possible mechanism for generating the electron-dominated current in TCS is the electron drift caused by its thermal anisotropy (e.g., Hau et al., 1993; Zelenyi et al., 2004). Such anisotropy is often observed in the magnetotail (e.g., Stiles et al., 1978; Walsh et al., 2011; Artemyev et al., 2014).

It has been unclear which of the two aforementioned mechanisms dominates the generation of TCS electron currents until recent global-scale hybrid (Lu et al., 2016) and particle-in-cell (Lu et al., 2018; Pritchett & Lu, 2018) simulations have suggested that the $\mathbf{E} \times \mathbf{B}$ drift of the magnetized electrons (the mostly unmagnetized ions do not $\mathbf{E} \times \mathbf{B}$ drift) in the presence of the TCS Hall electric field is the dominant mechanism contributing to the (predominantly electron) current density. These simulations also have found that the Hall electric field (E_z in the Geocentric Solar Magnetospheric, GSM, coordinate system or E_n, normal to the TCS plane) has a dawn-dusk asymmetry: it is stronger on the duskside than on the dawnside (see the global hybrid simulation results in Figures 1 and 2), indicating that the Hall effect is also stronger on the duskside. This occurs because more ions are demagnetized on the duskside because of the thinner current sheet and smaller B_z there, which, in turn, is caused by the dawnward transport of magnetic flux and plasma by the $\mathbf{E} \times \mathbf{B}$ drift in the Hall electric field. Such asymmetric current sheet has been linked to the more frequent occurrence of reconnection on the dusk side (Lin et al., 2014), which is critical to the pervasive asymmetry in many active time magnetotail phenomena (see reviews by Walsh et al., 2014, and Haaland et al., 2017, and references therein). However, systematic study of the Hall electric field E_z has so far been lacking, and there has been no observational confirmation of the dawn-dusk asymmetry of this field.

The E_z magnitude in the thin current sheet expected from simulations is on the order of 1 mV/m. Such a small electric field is difficult to measure by spacecraft with a spin axis along Z_{GSM}. In this paper, using two different, complimentary methods, we obtain the Hall electric field in Earth's magnetotail thin current sheet from MMS (Magnetospheric Multiscale) and THEMIS (Time History of Events and Macroscale Interactions during Substorm) spacecraft observations, respectively. More specifically, we investigate (1) whether the Hall electric

field exists in the magnetotail and has the direction and magnitude predicted by theory and simulations and (2) whether the Hall electric field is stronger on the duskside, as predicted by global-scale kinetic simulations (Lu et al., 2016, 2018). The data and the methods used to derive the Hall electric field are described in Section 2. The results are presented in Section 3, and the conclusions are given in Section 4.

2. Data and Methods

2.1. MMS

We use MMS and THEMIS observations to investigate the Hall electric field in Earth's magnetotail thin current sheet. During the MMS TCS crossings, the distances between the four spacecraft are small, so their measurements are similar. Therefore, we only use data from MMS1. For each TCS crossing selected, we determine the local normal coordinate system **l**, **m**, **n**, where the **l** axis is along the maximum variance eigenvector (Sonnerup & Scheible, 1998); the **m** axis is along the current density component $\mathbf{j}_\perp = \mathbf{j} - (\mathbf{j}\cdot\mathbf{l})\mathbf{l}$ (averaged over the entire current sheet crossing), which is perpendicular to **l**; and the **n** axis is directed perpendicular to **l** and **m**, i.e., $\mathbf{n} = \mathbf{l} \times \mathbf{m}$ (see details in Runov et al., 2005a).

The MMS observations (Burch et al., 2016) consist of 48 TCS crossings (or "events") by the spacecraft during the 2017 tail season (see Figure 3). These events are selected using the following criteria: (1) the peak current density is larger than 2.5 $\mathrm{nA/m^2}$, (2) the current sheet thickness is smaller than 1 R_E (for evaluation of the current sheet thickness, see Appendix A), (3) the current is flowing mainly in the dawn-dusk direction, (4) the crossing is at quiet-time with average flow speed smaller than 100 $\mathrm{km/s}$ (i.e., the current sheet that was observed during and right after magnetic reconnection is not adopted), and (5) the guide field B_m is not strong throughout the current sheet crossing, $B_m < 3B_n$, to exclude current sheets with strong

field-aligned current. The specific time periods of these events are listed in Table 1. We use the magnetic field from Fluxgate Magnetometer (FGM, Russell et al., 2016) and the plasma density, flow velocity, and temperature from Fast Plasma Instrument (FPI, Pollock et al., 2016).

Although MMS measure 3-D electric field directly (see, e.g., Ergun et al., 2016; Lindqvist et al., 2016), such direct measurement is reliable only when the magnitude of the electric field exceeds several mV/m in a very intense current sheet or during reconnection time (e.g., Wang et al., 2018; Torbert et al., 2018). However, according to the simulations, the magnitude of the Hall electric field is only on the order of 1 mV/m (Figures 1 and 2), so we cannot use direct electric field measurements. Therefore, to obtain the Hall electric field E_n from the MMS observations, we follow the method used in Tsai et al. (2017): In the magnetotail TCS, the electron flow in the **m** direction (V_{em}, predominantly perpendicular to the magnetic field) is contributed by three terms (e.g., Artemyev & Zelenyi, 2013, and references therein): (1) $\mathbf{E} \times \mathbf{B}$ drift velocity, (2) anisotropy drift because of finite electron pressure anisotropy $V_{e,ani} = -(\partial B_l/\partial n)(p_{e\parallel} - p_{e\perp})/(en_eB^2)$ (where $p_{e\parallel}$ and $p_{e\perp}$ are the parallel and perpendicular components of the electron pressure tensor), and (3) diamagnetic drift velocity $V_{e,DM} = B_l(\partial p_{e\perp}/\partial n)/(en_eB^2)$. By subtracting the other two terms from V_{em}, the $\mathbf{E} \times \mathbf{B}$ velocity can be written as

$$V_{E\times B} = V_{em} - V_{e,DM} - V_{e,ani}, \quad (1)$$

where, considering $\partial B_l/\partial n \approx \mu_0 j_m$, the two terms can be rewritten as

$$V_{e,ani} = -\mu_0 j_m(p_{e\parallel} - p_{e\perp})/(en_eB^2), \quad (2)$$

and

$$V_{e,DM} = \mu_0 B_l j_m(\partial p_{e\perp}/\partial B_l)/(en_eB^2). \quad (3)$$

To calculate $\partial p_{e\perp}/\partial B_l$, we fit $p_{e\perp}$ with a parabolic function $p_{e\perp} = \hat{p}_{e\perp}(1 - \alpha B_l^2)$, where $\hat{p}_{e\perp}$ and α are fitting constants. We obtain V_{em} and $j_m = en_e(V_{im} - V_{em})$ from direct measurements. The $\mathbf{E} \times \mathbf{B}$ drift is caused by the Hall electric field E_n and magnetic field B_l. Therefore, we obtain the Hall electric field from

$$E_n = V_{E\times B} B_l. \quad (4)$$

In the hybrid simulation results shown in Figure 2, the agreement between E_z and $V_{E\times B,y} B_x$ justifies the calculation of the Hall electric field using Equation (4) (E_z and $V_{E\times B,y} B_x$ equal to E_n and $V_{E\times B} B_l$, respectively, because in the simulation the current sheet is in the *x*-*y* plane).

2.2. THEMIS

As described above, we derive the Hall electric field indirectly for the MMS dataset. To measure the Hall electric field directly, we need to eliminate the effect of current sheet motion, which can generate motional electric fields that mask the direct measurements of E_z. However, the MMS events of thin current sheet are observed during the magnetotail flapping motion (e.g., Runov et al., 2005b, and references therein). Therefore, for direct measurements, we need to consider non-flapping current sheets, and the optimal circumstance for this is a slowly thinning current sheet. This thinning process takes about one hour and is characterized by a gradual current density increase (e.g., Petrukovich et al., 2013; Artemyev et al., 2016a). Direct electric field measurements by several spacecraft that observe such current sheet thinning at different distances from the equatorial plane (at different B_x) can be combined to reconstruct the profile of E_z. However, small separation of MMS spacecraft does not allow them to probe the thinning current sheet at different distances from the equator simultaneously. Yet we can apply this method to the THEMIS dataset. Therefore, we analyze one event in which four THEMIS spacecraft (Angelopoulos, 2008) observed current sheet thinning. Using multi-point magnetic field measurements (Auster et al., 2008), we obtain the

current density from the curlometer technique (Dunlop et al., 2002). The electric field E_z is obtained from the direct measurements of E_x and E_y (Bonnell et al., 2008) and by applying the approximation $\mathbf{E} \cdot \mathbf{B} = 0$.

3. Results

3.1. Single MMS Event

Figure 4 shows an example of the MMS magnetotail thin current sheet crossing events. Figure 4a shows the B_l, B_m, and B_n components of the magnetic field; the reversal of B_l at about 10:25:33 UT indicates current sheet crossing. The ion flow velocity is small in the entire time period (Figure 4c), which shows that this is a quiet-time current sheet crossing (i.e., the current sheet was not observed during or right after magnetic reconnection). Figure 4e shows electron, ion, and total current density in the **m** direction $j_{em} = -en_eV_{em}$, $j_{im} = en_eV_{im}$, and $j_m = j_{em} + j_{im}$ obtained from the direct measurements of density and velocity.

Figure 5 shows the MMS measurements versus B_l, a proxy of the distance to the neutral plane, for this TCS crossing event. The current density peaks at ~ 8 nA/m^2 at the center of the current sheet ($B_l = 0$), and it is mostly carried by electrons (Figure 5a). Figure 5c shows the electron pressure p_e and its parallel and perpendicular components, $p_{e\parallel}$, $p_{e\perp}$. The electron pressure has a parabolic shape with a maximum at the center ($B_l = 0$), and $p_{e\perp}$ is fitted with the parabolic function $p_{e\perp} = \hat{p}_{e\perp}(1 - \alpha B_l^2)$ as represented by the blue dashed line. The directly measured V_{em} has a peak at the current sheet center, about -300 km/s (Figure 5d). Figures 5e and 5f depict the electron anisotropy drift velocity $V_{e,ani}$ and the diamagnetic drift velocity $V_{e,DM}$ calculated using Equations (2) and (3), respectively, which shows that the contributions of these two drift velocities are small. By subtracting these two contributions from the total V_{em}, we obtain the $\mathbf{E} \times \mathbf{B}$ drift velocity (Equation (1)) with a magnitude of

about 250 km/s, as plotted in Figure 5g. Figure 5h shows the profile of the Hall electric field E_n calculated using Equation (4). The Hall electric field has a bipolar structure (pointing toward the center of the current sheet), and its magnitude is on the order of 1 mV/m.

The MMS current sheet crossing event shows that the electron current is mostly contributed by the electron $\mathbf{E} \times \mathbf{B}$ drift in the **m** direction, i.e., the contribution from the anisotropy drift due to the electron pressure anisotropy is small. However, even 1% to 10% of the electron pressure anisotropy can result in strong electron current density (Zelenyi et al., 2011; Artemyev and Zelenyi, 2013). In our MMS event list, there are three events of this type (indicated by asterisks in Table 1) in which the electron current density is mostly contributed by the anisotropy drift, i.e., $V_{em} \approx V_{e,ani}$. Figure 6 shows a sample event of this type. In this TCS crossing, the current is still mainly carried by electrons, but the electron current is caused mostly by the anisotropy drift rather than the $\mathbf{E} \times \mathbf{B}$ drift. The anisotropy drift velocity contributes about 3/4 of the V_{em} in this event (see Figures 6d and 6f). Therefore, the $\mathbf{E} \times \mathbf{B}$ drift velocity and the Hall electric field E_n are not strong in this event.

3.2. MMS Statistics and Dawn-Dusk Asymmetry

Previous global-scale hybrid simulations (Lu et al., 2016) and particle-in-cell simulations (Lu et al., 2018) have shown that the Hall effect in the magnetotail is stronger on the duskside, as indicated by the stronger Hall electric field on the duskside. Figures 1 and 2 show the global hybrid simulation results of the Hall electric field in the magnetotail thin current sheet using AuburN Global hybrId codE in 3-D (ANGIE3D, for details of the simulation model, see Lin et al., 2014, 2017). The Hall electric field E_z at $x = -20R_E$ is stronger on the duskside ($y = 10R_E$) than on the dawnside ($y = -10R_E$). We perform a statistical study using the 48

MMS TCS crossing events to check the dawn-dusk asymmetry of the Hall electric field magnitude and to determine whether it is consistent with the simulation results.

Of the 48 MMS TCS crossing events, 23 are on the dawnside and 25 on the duskside. Among the 48 MMS events shown in Table 1, there are three events (on the duskside) in which the electron flow velocity is mostly contributed by the anisotropy drift (caused by electron pressure anisotropy) rather than the $\mathbf{E} \times \mathbf{B}$ drift (for example, the event shown in Figure 6). The statistical result of the MMS events is shown in Figure 7, in which the red curves represent the statistical result of all the events, and the blue curves represent the statistical result of the events in which the $\mathbf{E} \times \mathbf{B}$ drift dominates the electron velocity (i.e., the strong anisotropy events are excluded). For both situations, the magnitude of E_n is larger on the duskside, especially when the events with strong anisotropy causing large anisotropy drift are excluded. Overall, on the duskside the average magnitude of E_n is about 0.5 mV/m, and on the dawnside the average magnitude is lower, about 0.25 mV/m.

In the three events with dominating electron anisotropy drift, the $\mathbf{E} \times \mathbf{B}$ drift velocity is very small, usually around zero, as shown in Figure 6. This small $\mathbf{E} \times \mathbf{B}$ drift velocity gives a small Hall electric field magnitude. These values of $\mathbf{E} \times \mathbf{B}$ drift velocity and Hall electric field are smaller than average magnitudes. Nevertheless, this is based on only three events of this kind, we cannot rule out the possibility of current sheets with a strong $\mathbf{E} \times \mathbf{B}$ drift and an even stronger anisotropy drift. Further investigations are needed to better understand this issue. Also note that compared to the above average magnitudes from the MMS statistics, the ANGIE3D simulation (as shown in Figures 1 and 2) gives a larger magnitude of the Hall electric field. This is because the simulation considers an extreme case with strong driving, i.e., a fast solar wind speed ($700\ \mathrm{km/s}$) and a strong southward interplanetary magnetic field

(-10 nT), while the observation result is averaged over various solar wind and interplanetary magnetic field conditions.

3.3. THEMIS measurements in thinning current sheet

To investigate the profile of E_z based on direct electric field measurements, we analyze THEMIS spacecraft observations shown in Figure 8. The four THEMIS spacecraft (ThA, ThC, ThD, ThE) formed a tetrahedron with sides about a few R_E in the nightside magnetotail (near midnight, radial distance about 12 R_E). The spacecraft ThD, ThC, and ThE were well separated in the GSM *x*-*y* plane. ThD and ThC were located above the equatorial plane (the corresponding $B_x > 0$), and ThA was located far below the equatorial plane ($B_x < 0$). All four spacecraft observed a gradual B_z decrease and a j_y increase (because the spacecraft separation is on the order of R_E, the measured j_y should be interpreted as a spatially-averaged value). The spacecraft configuration separated around the equatorial plane allows us to simultaneously measure the electric field at different B_x (different distances from the equator) in such a stationary thinning current sheet (without TCS flapping motion).

The interval of current sheet thinning shown in Figure 8 was embedded in a long time interval (~5 hours) of substorm activities that includes four weak substorms (four well separated peaks of AE index) and about four subintervals of current sheet thinning (characterized by gradual B_z decreases) ended by dipolarizations (characterized by rapid B_z increases). This long time interval is plotted in Figure 9. Each dipolarization was accompanied by fast plasma flows with a significant earthward component. Such flows indicate that THEMIS spacecraft were located earthward of the magnetic reconnection region (e.g., Baker et al. 1996; Angelopoulos et al., 2013). During the subinterval shown in Figure 8, the spacecraft configuration was optimal for calculation of current density j_y and for

measurement of electric field at different distances from the equatorial plane. The increase of current density j_y confirms thinning of the current sheet (see Figure 8c).

Because the THEMIS spacecraft measure electric fields within the spin plane, we apply the approximation $\mathbf{E} \cdot \mathbf{B} = 0$ to reconstruct the 3-D electric field distribution and estimate the E_z component. This approximation requires that the B_z/B_x ratio be not too small, and thus it cannot be justified for ThA. Moreover, the anisotropic electron population in thin current sheets can generate field-aligned quasi-steady electric fields violating the $\mathbf{E} \cdot \mathbf{B} = 0$ approximation (e.g., see discussion in Artemyev et al., 2016b). Therefore, the E_z field derived using this approximation should be considered as a leading order estimate. The noisiest field was measured by ThC, which was located farthest from the equatorial plane. The electric field E_z is calculated for the three THEMIS spacecraft (ThC, ThD, ThE) and shows polarity and magnitude consistent with the MMS statistics – directed toward the equatorial plane and several tenths of 1 mV/m (see Figure 8f).

4. Conclusions

Systematic observations of the Hall electric field in quiet-time magnetotail thin current sheet were performed using MMS and THEMIS measurements. The MMS observations at about $20\,R_E$ were used to derive the Hall electric field E_n indirectly from the magnetic field and plasma measurements; electric field measurements (in the spin plane) from THEMIS at about $12\,R_E$ were used to calculate E_n directly under the approximation $\mathbf{E} \cdot \mathbf{B} = 0$. These two different observations using two spacecraft missions both showed that the Hall electric field E_n has a bipolar structure across the current sheet directed towards the center of the current sheet, and the typical magnitude of this field is several tenths of 1 mV/m. The statistics using MMS magnetotail TCS events showed a clear dawn-dusk asymmetry of the E_n magnitude,

stronger on the duskside, which confirms predictions from previous global-scale hybrid and particle-in-cell simulations.

Appendix A: Determination of Magnetotail Thin Current Sheet Thickness

Only thin current sheet with thickness L smaller than 1 R_E is considered in this study. The thickness is estimated using $B_0/(\mu_0 j_0)$, where B_0 is the magnetic field magnitude at the current sheet boundary, and j_0 is the peak value of the cross-tail current density j_m. Because the orbit of MMS is equatorial, the spacecraft often do not reach the thin current sheet boundary with $|B_l| = B_0$. Therefore, we use the estimate $B_0 = 0.3B_{lobe}$ based on previous investigations of the magnetotail thin current sheet by Cluster spacecraft (e.g., Artemyev et al., 2011; Petrukovich et al. 2015), where B_{lobe} is the magnitude of lobe magnetic field evaluated using pressure balance, i.e., $B_{lobe} = \left(B_x^2 + B_y^2 + 2\mu_0 p_p\right)^{1/2}$, and $p_p = k_B(n_e T_e + n_i T_i)$. The accuracy of this estimate is about 30% (most of the thin current sheets from the Cluster dataset have $B_0 \in [0.2,0.5]B_{lobe}$, see Figure 6 in Petrukovich et al., 2015 and Figure 4 in Artemyev et al., 2011). Using this method, we estimate the current sheet thickness in the 48 events in Table 1, as plotted in Figure A1 as function of peak cross-tail current density. The thickness is within 2000 km (even for $B_0 = 0.5B_{lobe}$, the thickness would be within 4000 km) and on the order of several local ion inertial length (d_i, evaluated using peak ion density), showing that the current sheets considered in this study are indeed thin current sheet.

Acknowledgments

This work was supported by NASA contract NAS5-02099 and by NASA grants NNX17AI46G and 80NSSC18K1122. We would like to thank the following people specifically C. W. Carlson and J. P. McFadden for the use of ESA data, D. E. Larson and R.

P. Lin for the use of SST data, and K. H. Glassmeier, U. Auster, and W. Baumjohann for the use of FGM data provided under the lead of the Technical University of Braunschweig and with financial support through the German Ministry for Economy and Technology and the German Aerospace Center (DLR) under contract 50 OC 0302. We thank Q. M. Lu, H. S. Fu, Y. V. Khotyaintsev, and O. Le Contel for useful discussion. We thank J. Hohl for editorial assistance. The specific time periods of all the spacecraft observation events are listed in Table 1, and the corresponding MMS and THEMIS data can be downloaded from http://lasp.colorado.edu/mms/sdc and http://themis.ssl.berkeley.edu, respectively. The AuburN Global hybrId CodE in 3-D (ANGIE3D, see Lin et al., 2014, 2017) results are generated from our computer simulation model. The simulation data used to plot Figures 1 and 2 can be obtained at https://www.dropbox.com/s/oeqm8z5fj4lozgv/fieldfine0160.dat?dl=0. The computer resources were provided by the NASA High-End Computing (HEC) Program through the NASA Advanced Supercomputing (NAS) Division at Ames Research Center.

References

Angelopoulos, V. (2008). The THEMIS Mission. *Space Science Reviews*, *141*, 5-34. http://doi.org/10.1007/s11214-008-9336-1

Angelopoulos, V., Runov, A., Zhou, X.-Z., Turner, D. L., Kiehas, S. A., Li, S.-S., & Shinohara, I. (2013). Electromagnetic Energy Conversion at Reconnection Fronts. *Science*, *341*, 1478-1482, http://doi.org/10.1126/science.1236992

Artemyev, A., & Zelenyi, L. (2013). Kinetic Structure of Current Sheets in the Earth Magnetotail. *Space Science Reviews*, *178*, 419-440. http://doi.org/10.1007/s11214-012-9954-5

Artemyev, A. V., Angelopoulos, V., Runov, A., & Petrukovich, A. A. (2016a). Properties of current sheet thinning at x~10 to 12 R_E. *Journal of Geophysical Research Space Physics*, *121*, 6718-6731. http://doi.org/10.1002/2016JA022779

Artemyev, A. V., Angelopoulos, V., Runov, A., & Zelenyi, L. M. (2016b). Earthward electric field and its reversal in the near-Earth current sheet. *Journal of Geophysical Research Space Physics*, *121*, 10803-10812. http://doi.org/10.1002/2016ja023200

Artemyev, A. V., Petrukovich, A. A., Nakamura, R., & Zelenyi, L. M. (2011). Cluster statistics of thin current sheets in the Earth magnetotail: Specifics of the dawn flank, proton temperature profiles and electrostatic effects. *Journal of Geophysical Research Space Physics*, *116*, A09233. http://doi.org/10.1029/2011ja016801

Artemyev, A. V., Petrukovich, A. A., Zelenyi, L. M., Nakamura, R., Malova, H. V., & Popov, V. Y. (2009). Thin embedded current sheets: Cluster observations of ion kinetic structure and analytical models. *Annales Geophysicae*, *27*, 4075-4087. http://doi.org/10.5194/angeo-27-4075-2009

Artemyev, A. V., Walsh, A. P., Petrukovich, A. A., Baumjohann, W., Nakamura, R., & Fazakerley, A. N. (2014). Electron pitch angle/energy distribution in the magnetotail. *Journal of Geophysical Research Space Physics*, *119*, 7214-7227. http://doi.org/10.1002/2014ja020350

Aunai, N., Belmont, G., & Smets, R. (2011). Proton acceleration in antiparallel collisionless magnetic reconnection: Kinetic mechanisms behind fluid dynamics. *Journal of Geophysical Research Space Physics*, *116*, A09232. http://doi.org/10.1029/2011JA016688

Auster, H. U., Glassmeier, K. H., Magnes, W., Aydogar, O., Baumjohann, W., Constantinescu, D., . . . Wiedemann, M. (2008). The THEMIS Fluxgate Magnetometer. *Space Science Reviews*, *141*, 235-264. http://doi.org/10.1007/s11214-008-9365-9

Baker, D. N., Pulkkinen, T. I., Angelopoulos, V., Baumjohann, W., & McPherron, R. L. (1996). Neutral line model of substorms: Past results and present view. *Journal of Geophysical Research Space Physics*, *101*, 12975-13010. http://doi.org/10.1029/95JA03753

Birn, J., Schindler, K., & Hesse, M. (2004). Thin electron current sheets and their relation to auroral potentials. *Journal of Geophysical Research Space Physics*, *109*, A02217. http://doi.org/10.1029/2003ja010303

Bonnell, J. W., Mozer, F. S., Delory, G. T., Hull, A. J., Ergun, R. E., Cully, C. M., . . . Harvey, P. R. (2008). The Electric Field Instrument (EFI) for THEMIS. *Space Science Reviews*, *141*, 303-341. http://doi.org/10.1007/s11214-008-9469-2

Burch, J. L., Moore, T. E., Torbert, R. B., & Giles, B. L. (2016). Magnetospheric Multiscale Overview and Science Objectives. *Space Science Reviews*, *199*, 5-21. http://doi.org/10.1007/s11214-015-0164-9

Dunlop, M. W., Balogh, A., Glassmeier, K. H., & Robert, P. (2002). Four-point Cluster application of magnetic field analysis tools: The Curlometer. *Journal of Geophysical Research Space Physics*, *107*(A11), 1384. http://doi.org/10.1029/2001ja005088

Dunlop, M. W., Balogh, A., Glassmeier, K. H., & Robert, P. (2002). Four-point Cluster application of magnetic field analysis tools: The Curlometer. *Journal of Geophysical Research Space Physics*, *107*(A11), 1384. http://doi.org/10.1029/2001ja005088

Ergun, R. E., Tucker, S., Westfall, J., Goodrich, K. A., Malaspina, D. M., Summers, D., . . . Cully, C. M. (2016). The Axial Double Probe and Fields Signal Processing for the MMS Mission. *Space Science Review, 199*, 167-188. http://doi.org/10.1007/s11214-014-0115-x

Fu, X. R., Lu, Q. M., & Wang, S. (2006). The process of electron acceleration during collisionless magnetic reconnection. *Physics of Plasmas, 13*, 012309. http://doi.org/10.1063/1.2164808

Haaland, S., Runov, A., & Forsyth, C. (2017). *Dawn-dusk asymmetries in planetary plasma environments*. Hoboken, NJ: John Wiley & Sons. http://doi.org/10.1002/9781119216346

Hau, L. N., Phan, T. D., Sonnerup, B. U. O., & Paschmann, G. (1993). Double-Polytropic Closure in the Magnetosheath. *Geophysical Research Letters*, *20*(20), 2255-2258. http://doi.org/10.1029/93gl02491

Hesse, M., Winske, D., & Birn, J. (1998). On the ion-scale structure of thin current sheets in the magnetotail. *Physica Scripta*, *T74*, 63-66. http://doi.org/10.1088/0031-8949/1998/T74/012

Korovinskiy, D. B., Semenov, V. S., Erkaev, N. V., Divin, A. V., Biernat, H. K., & Möstl, U. V. (2011). A 2.5-D electron Hall-MHD analytical model of steady state Hall magnetic reconnection in a compressible plasma. *Journal of Geophysical Research*, *116*, A05219. http://doi.org/10.1029/2010JA015942

Lin, Y., Wing, S., Johnson, J. R., Wang, X. Y., Perez, J. D., & Cheng, L. (2017). Formation and transport of entropy structures in the magnetotail simulated with a 3-D global hybrid code. *Geophysical Research Letters*, *44*, 5892-5899. http://doi.org/10.1002/2017GL073957

Lin, Y., Wang, X. Y., Lu, S., Perez, J. D., & Lu, Q. (2014). Investigation of storm time magnetotail and ion injection using three-dimensional global hybrid simulation. *Journal of Geophysical Research Space Physics*, *119*, 7413-7432. http://doi.org/10.1002/2014JA020005

Lindqvist, P.-A., Olsson, G., Torbert, R. B., King, B., Granoff, M., Rau, D., . . . Tucker, S. (2016). The Spin-Plane Double Probe Electric Field Instrument for MMS. *Space Science Review, 199*, 137-165. http://doi.org/10.1007/s11214-014-0116-9

Liu, Y.-H., Birn, J., Daughton, W., Hesse, M. & Schindler, K. (2014). Onset of reconnection in the near magnetotail: PIC simulations. *Journal of Geophysical Research Space Physics*, *119*, 9773-9789. http://doi.org/10.1002/2014JA020492

Lu, Q. M., Huang, C., Xie, J. L., Wang, R. S., Wu, M. Y., Vaivads, A., & Wang, S. (2010). Features of separatrix regions in magnetic reconnection: Comparison of 2-D particle-in-cell simulations and Cluster observations. *Journal of Geophysical Research Space Physics*, *115*, A11208. http://doi.org/10.1029/2010ja015713

Lu, S., Lin, Y., Angelopoulos, V., Artemyev, A. V., Pritchett, P. L., Lu, Q. M., & Wang, X. Y. (2016). Hall effect control of magnetotail dawn-dusk asymmetry: A three-dimensional global hybrid simulation. *Journal of Geophysical Research Space Physics*, *121*, 11882-11895. http://doi.org/10.1002/2016ja023325

Lu, S., Pritchett, P. L., Angelopoulos, V., & Artemyev, A. V. (2018). Formation of Dawn-Dusk Asymmetry in Earth's Magnetotail Thin Current Sheet: A Three-Dimensional Particle-In-Cell Simulation. *Journal of Geophysical Research Space Physics*, *123*, 2801-2814. http://doi.org/10.1002/2017ja025095

Nagai, T., Shinohara, I., Fujimoto, M., Hoshino, M., Saito, Y., Machida, S., & Mukai, T. (2001). Geotail observations of the Hall current system: Evidence of magnetic reconnection in the magnetotail. *Journal of Geophysical Research Space Physics*, *106*(A11), 25929-25949. http://doi.org/10.1029/2001ja900038

Petrukovich, A., Artemyev, A. V., Nakamura, R., Panov E. V., & Baumjohann, W. (2013). Cluster observations of dBz/dx during growth phase magnetotail stretching intervals.

Journal of Geophysical Research Space Physics, *118*, 5720-5730. http://doi.org/10.1002/jgra.50550

Petrukovich, A., Artemyev, A., Vasko, I., Nakamura, R., & Zelenyi, L. (2015). Current Sheets in the Earth Magnetotail: Plasma and Magnetic Field Structure with Cluster Project Observations. *Space Science Reviews*, *188*, 311-337. http://doi.org/10.1007/s11214-014-0126-7

Pollock, C., Moore, T., Jacques, A., Burch, J., Gliese, U., Saito, Y., . . . Zeuch, M. (2016). Fast Plasma Investigation for Magnetospheric Multiscale. *Space Science Reviews*, *199*, 331-406. http://doi.org/10.1007/s11214-016-0245-4

Pritchett, P. L., & Coroniti, F. V. (1994). Convection and the Formation of Thin Current Sheets in the near-Earth Plasma Sheet. *Geophysical Research Letters*, *21*(15), 1587-1590. http://doi.org/10.1029/94gl01364

Pritchett, P. L., & Lu, S. (2018). Externally Driven Onset of Localized Magnetic Reconnection and Disruption in a Magnetotail Configuration. *Journal of Geophysical Research Space Physics*, *123*, 2787-2800. http://doi.org/10.1002/2017ja025094

Runov, A., Sergeev, V. A., Nakamura, R., Baumjohann, W., Apatenkov, S., Asano, Y., . . . Balogh, A. (2006). Local structure of the magnetotail current sheet: 2001 Cluster observations. *Annales Geophysicae*, *24*, 247-262. http://doi.org/10.5194/angeo-24-247-2006

Runov, A., Sergeev, V. A., Nakamura, R., Baumjohann, W., Zhang, T. L., Asano, Y., . . . Reme, H. (2005a). Reconstruction of the magnetotail current sheet structure using multi-point Cluster measurements. *Planetary and Space Science*, *53*, 237-243. http://doi.org/10.1016/j.pss.2004.09.049

Runov, A., Sergeev, V. A., Baumjohann, W., Nakamura, R., Apatenkov, S., Asano, Y., . . . Reme, H. (2005b). Electric current and magnetic field geometry in flapping magnetotail

current sheets. *Annales Geophysicae*, *23*, 1391-1403. http://doi.org/10.5194/angeo-23-1391-2005

Russell, C. T., Anderson, B. J., Baumjohann, W., Bromund, K. R., Dearborn, D., Fischer, D., . . . Richter, I. (2016). The Magnetospheric Multiscale Magnetometers. *Space Science Reviews*, *199*, 189-256. http://doi.org/10.1007/s11214-014-0057-3

Schindler, K., Birn, J., & Hesse, M. (2012). Kinetic model of electric potentials in localized collisionless plasma structures under steady quasi-gyrotropic conditions. *Physics of Plasmas*, *19*, 082904. http://doi.org/10.1063/1.4747162

Sitnov, M. I., & Merkin, V. G. (2016), Generalized magnetotail equilibria: Effects of the dipole field, thin current sheets, and magnetic flux accumulation, *Journal of Geophysical Research Space Physics*, *121*, 7664-7683. http://doi.org/10.1002/2016JA023001

Sonnerup, B. U. Ö. (1979). Magnetic field reconnection, in Solar System Plasma Physics, edited by L. J. Lanzerotti, C. F. Kennel, and E. N. Parker, vol. 3, pp. 45-108, North-Holland, New York.

Sonnerup, B. U. Ö., & Scheible, M. (1998). Minimum and maximum vaiance analysis, in *Analysis Methods for Multi-Spacecraft Data*, edited by G. Paschmann and P. W. Daly, pp. 185-220, Int. Space Sci. Inst., Bern, Switzerland.

Stiles, G. S., Hones, E. W., Bame, S. J., & Asbridge, J. R. (1978). Plasma Sheet Pressure Anisotropies. *Journal of Geophysical Research Space Physics*, *83*, 3166-3172. http://doi.org/10.1029/JA083iA07p03166

Torbert, R. B., Burch, J. L., Phan, T. D., Hesse, M., Argall, M. R., Shuster, J, . . . Saito, Y. (2018). Electron-scale dynamics of the diffusion region during symmetric magnetic reconnection in space. *Science*. http://doi.org/10.1126/science.aat2998

Tsai, E., Artemyev, A. V., & Angelopoulos, V. (2017). Ion motion in a polarized current sheet. *Physics of Plasmas*, *24*, 012908. http://doi.org/10.1063/1.4975017

Vasko, I. Y., Artemyev, A. V., Petrukovich, A. A., Nakamura, R., & Zelenyi, L. M. (2014). The structure of strongly tilted current sheets in the Earth magnetotail. *Annales Geophysicae*, *32*, 133-146. http://doi.org/10.5194/angeo-32-133-2014

Walsh, A. P., Owen, C. J., Fazakerley, A. N., Forsyth, C., & Dandouras, I. (2011). Average magnetotail electron and proton pitch angle distributions from Cluster PEACE and CIS observations. *Geophysical Research Letters*, *38*, L06103. http://doi.org/10.1029/2011gl046770

Walsh, A. P., Haaland, S., Forsyth, C., Keesee, A. M., Kissinger, J., Li, K., . . . Taylor, M. G. G. T. (2014). Dawn-dusk asymmetries in the coupled solar wind-magnetosphere-ionosphere system: A review. *Annales Geophysicae*, *32*, 705-737. http://doi.org/10.5194/angeo-32-705-2014

Wang, R. S., Lu, Q. M., Nakamura, R., Baumjohann, W., Huang, C., Russell, C. T., . . . Giles, B. (2018). An Electron-Scale Current Sheet Without Bursty Reconnection Signatures Observed in the Near-Earth Tail. *Geophysical Research Letters*, *45*, 4542-4549. http://doi.org/10.1002/2017gl076330

Wygant, J. R., Cattell, C. A., Lysak, R., Song, Y., Dombeck, J., McFadden, J., . . . Mouikis, C. (2005). Cluster observations of an intense normal component of the electric field at a thin reconnecting current sheet in the tail and its role in the shock-like acceleration of the ion fluid into the separatrix region. *Journal of Geophysical Research Space Physics*, *110*, A09206. http://doi.org/10.1029/2004ja010708

Zelenyi, L. M., Malova, H. V., Artemyev, A. V., Popov, V. Y., & Petrukovich, A. A. (2011). Thin current sheets in collisionless plasma: Equilibrium structure, plasma instabilities, and particle acceleration. *Plasma Physics Reports*, *37*, 118-160. http://doi.org/10.1134/S1063780x1102005x

Zelenyi, L. M., Malova, H. V., Popov, V. Yu., Delcourt, D., & Sharma, A. S. (2004). Nolinear equilibrium structure of thin currents sheets: influence of electron pressure annisotropy. *Nolinear Processes in Geophysics*, *11*, 579-587.

Table 1. Event list (TCS crossings by MMS)
(Note: In the events marked with asterisks, the electron flow velocity is mostly contributed by the anisotropy drift originated from the electron pressure anisotropy rather than the $\mathbf{E} \times \mathbf{B}$ drift.)

Date and time	$X_{GSM}(R_E)$	$Y_{GSM}(R_E)$
2017-06-02/12:25:00-13:00:00	-18.34	-6.89
2017-06-02/22:21:30-22:27:00	-20.85	-11.69
2017-06-03/04:45:30-04:48:00	-20.87	-13.37
2017-06-03/05:44:10-05:49:00	-20.78	-13.46
2017-06-05/12:17:10-12:19:00	-20.3	-7.9
2017-06-06/03:10:00-03:16:00	-21.07	-13.27
2017-06-06/08:08:00-08:09:30	-19.97	-13.2
2017-06-06/08:15:00-08:18:00	-19.93	-13.19
2017-06-08/05:29:00-05:32:30	-19.99	-6.53
2017-06-08/07:04:00-07:10:00	-20.55	-7.02
2017-06-08/12:15:00-12:23:00	-21.73	-8.61
2017-06-08/20:32:00-20:35:00	-21.88	-12.06
2017-06-09/00:40:00-00:50:00	-21.23	-12.91
2017-06-09/01:20:30-01:26:00	-21.09	-12.98
2017-06-09/03:11:00-03:17:00	-20.62	-13.06
2017-06-13/20:52:00-20:57:00	-20.8	-5.5
2017-06-13/21:09:00-21:11:00	-20.89	-5.61
2017-06-13/22:15:00-22:17:30	-21.28	-6.08
2017-06-14/00:57:00-01:00:00	-22.04	-7.03
2017-06-14/01:59:00-02:05:00	-22.27	-7.32
2017-06-17/04:05:00-04:07:00	-23.23	-7.98
2017-06-19/09:10:00-09:25:00	-20.22	-1.88
2017-06-20/03:15:30-03:17:30	-23.36	-7.94
2017-08-01/11:39:20-11:41:00	-22.4	8.26
2017-08-03/08:06:00-08:07:20	-18.51	12.16
2017-08-04/16:03:00-16:06:00	-19.1	5.54
2017-08-04/16:10:00-16:14:00	-19.04	5.46
2017-08-09/07:30:00-07:35:00	-20.61	13.62
2017-08-12/01:18:00-01:21:00	-19.61	14.39
2017-08-15/17:45:00-17:48:00*	-19.21	10.06
2017-08-18/16:56:00-16:59:00*	-17.41	9.04
2017-08-20/10:24:00-10:27:00	-17.41	16.64
2017-08-23/12:48:00-12:51:30	-18.29	16.92
2017-08-25/16:08:00-16:10:00	-12.21	17.15
2017-08-25/20:12:40-20:15:40	-14.12	18.19
2017-08-25/20:52:00-20:55:00	-14.39	18.25
2017-08-26/17:58:45-18:00:20*	-17.96	15.24
2017-08-29/06:40:00-06:41:30	-17.16	17.93
2017-08-29/18:41:00-18:43:00	-16.55	13.49
2017-08-29/20:10:00-20:20:00	-16.17	12.5
2017-09-01/01:00:00-01:07:00	-16.29	18.9
2017-09-01/01:25:30-01:27:00	-16.33	18.83
2017-07-03/05:52:00-05:54:00	-17.91	3.26
2017-07-12/00:15:00-00:25:00	-22.26	3.83
2017-07-12/11:11:00-11:16:00	-24.51	3.11
2017-07-12/14:10:00-14:14:00	-24.47	2.24
2017-07-20/07:45:00-07:46:40	-20.54	7.95
2017-07-22/21:22:00-21:25:00	-16.78	8.45

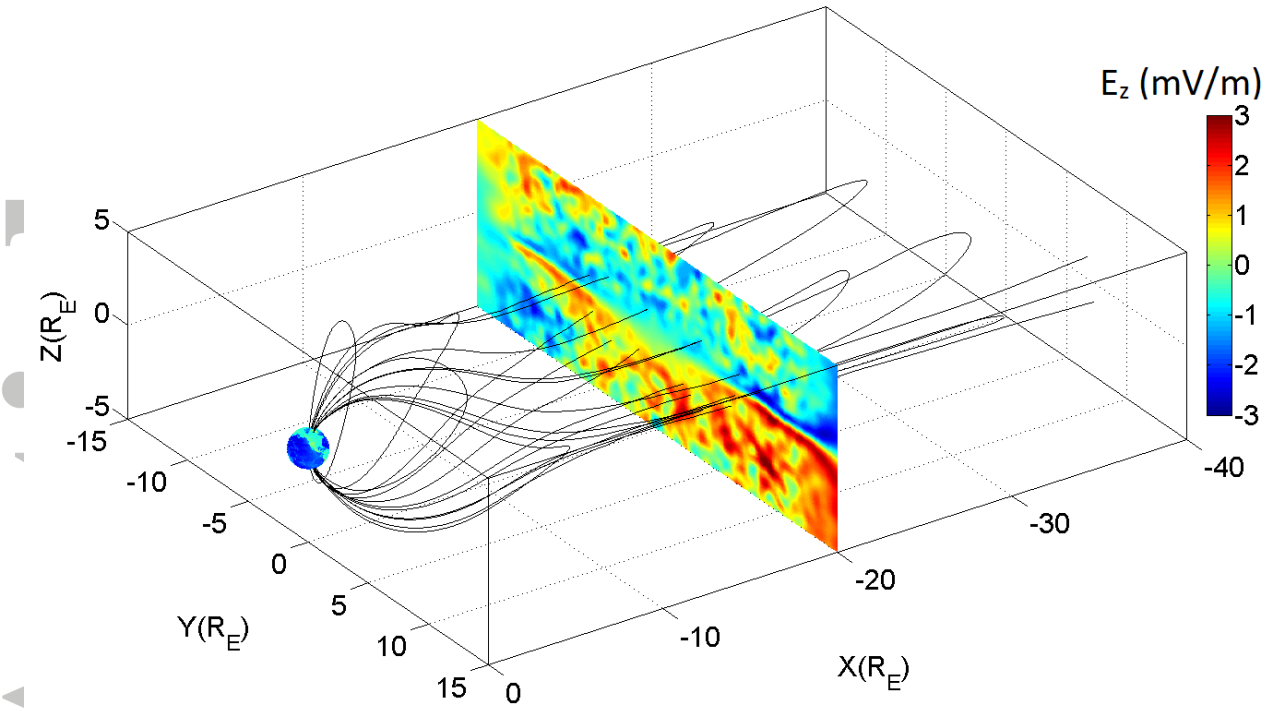

Figure 1. Global hybrid simulation result of AuburN Global hybrId CodE in 3-D (ANGIE3D) showing the configuration of magnetic field lines and the contour of Hall electric field E_z at $x = -20R_E$ at $t = 1144$ s. The simulation uses a pure southward interplanetary magnetic field (IMF), -10 nT, and a steady solar wind speed in the x direction, -700 km/s. The structure of the magnetotail (characterized by stretched field lines) forms self-consistently via interaction between the IMF/solar wind and the geomagnetic field. The Hall electric field E_z forms in the magnetotail thin current sheet. For more details of the simulation model, see Lin et al. (2014, 2017).

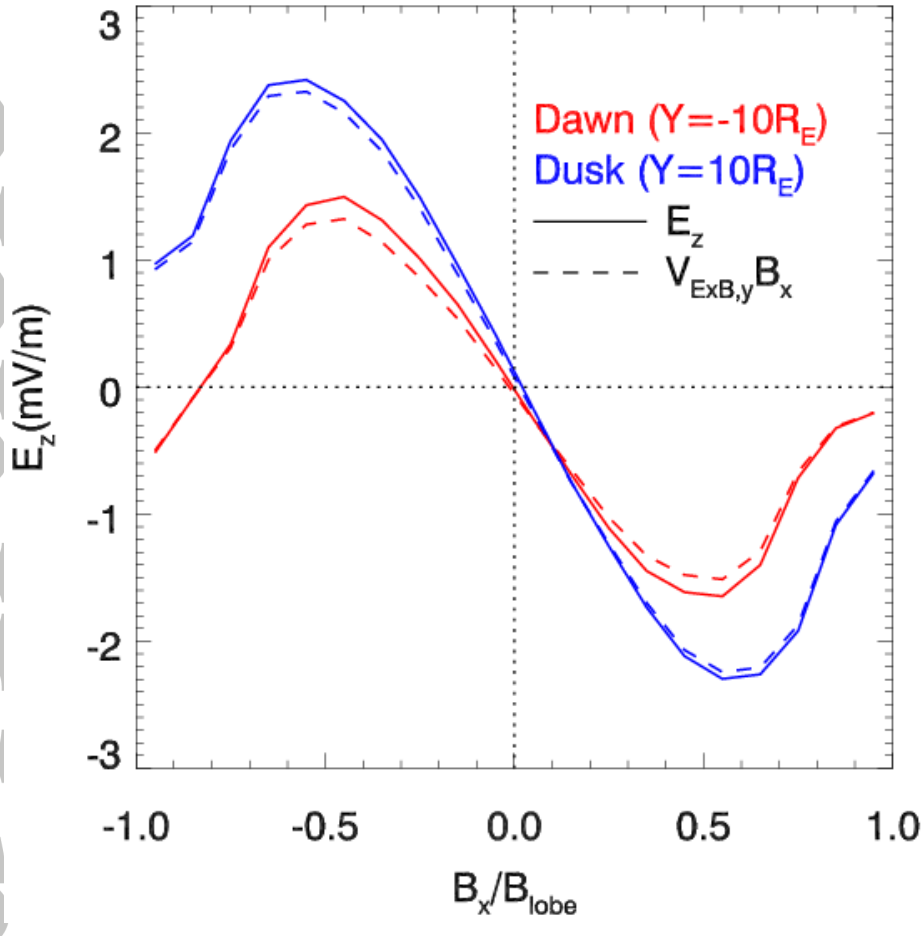

Figure 2. Profiles of the Hall electric field E_z from ANGIE3D at $x = -20R_E$ on the duskside ($y = 10R_E$) and the dawnside ($y = -10R_E$) at $t = 1144$ s. The dashed curves represent the electric field calculate using $E_z = V_{E\times B,y}B_x$, where $V_{E\times B,y} = (E_zB_x - E_xB_z)/B^2$. The magnetic field B_x indicates the distance to the center of the current sheet, and it is normalized to the magnitude of the lobe magnetic field B_{lobe} (we use plasma pressure at the current sheet center to calculate B_{lobe} from the pressure balance).

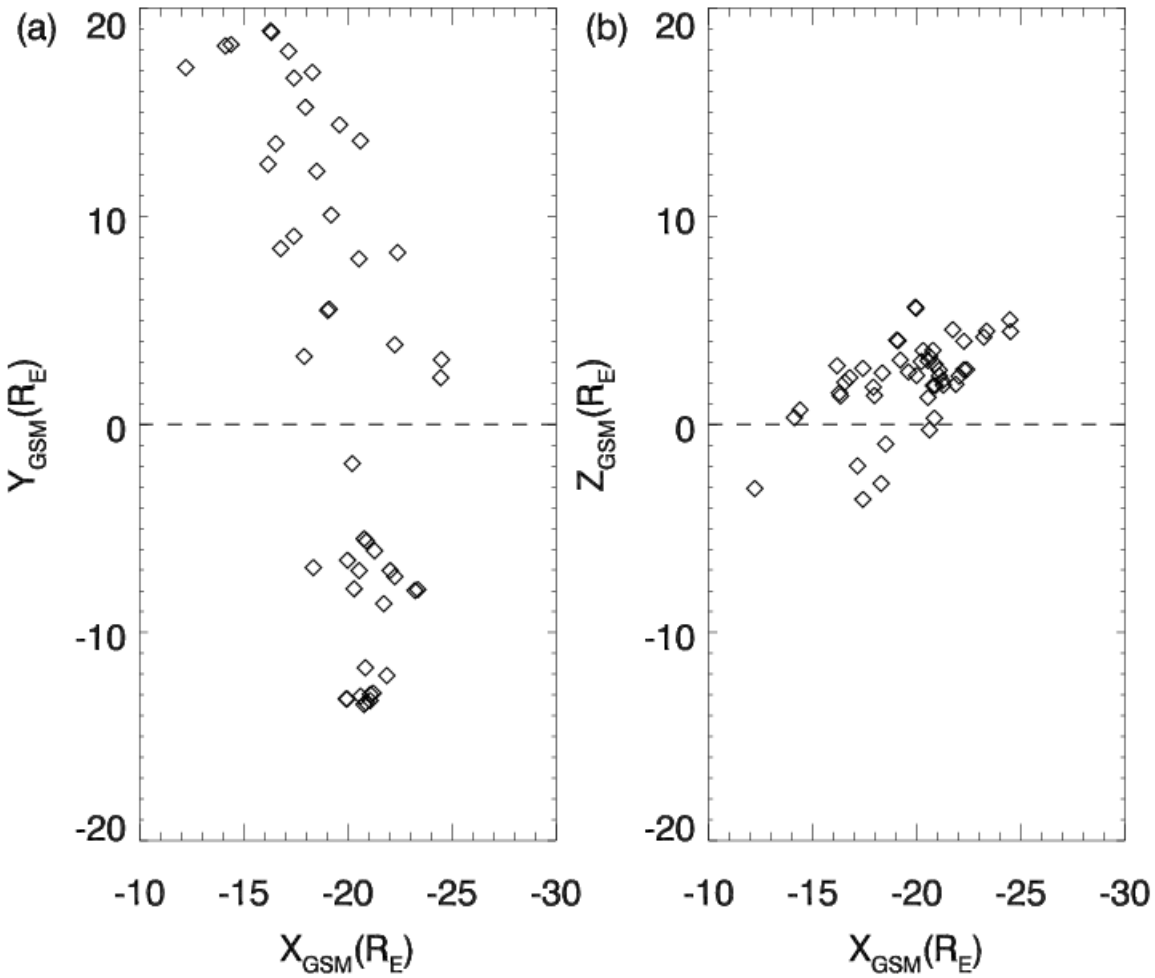

Figure 3. Location of the TCS events observed by MMS in the (a) GSM *x-y* plane and (b) GSM *x-z* plane.

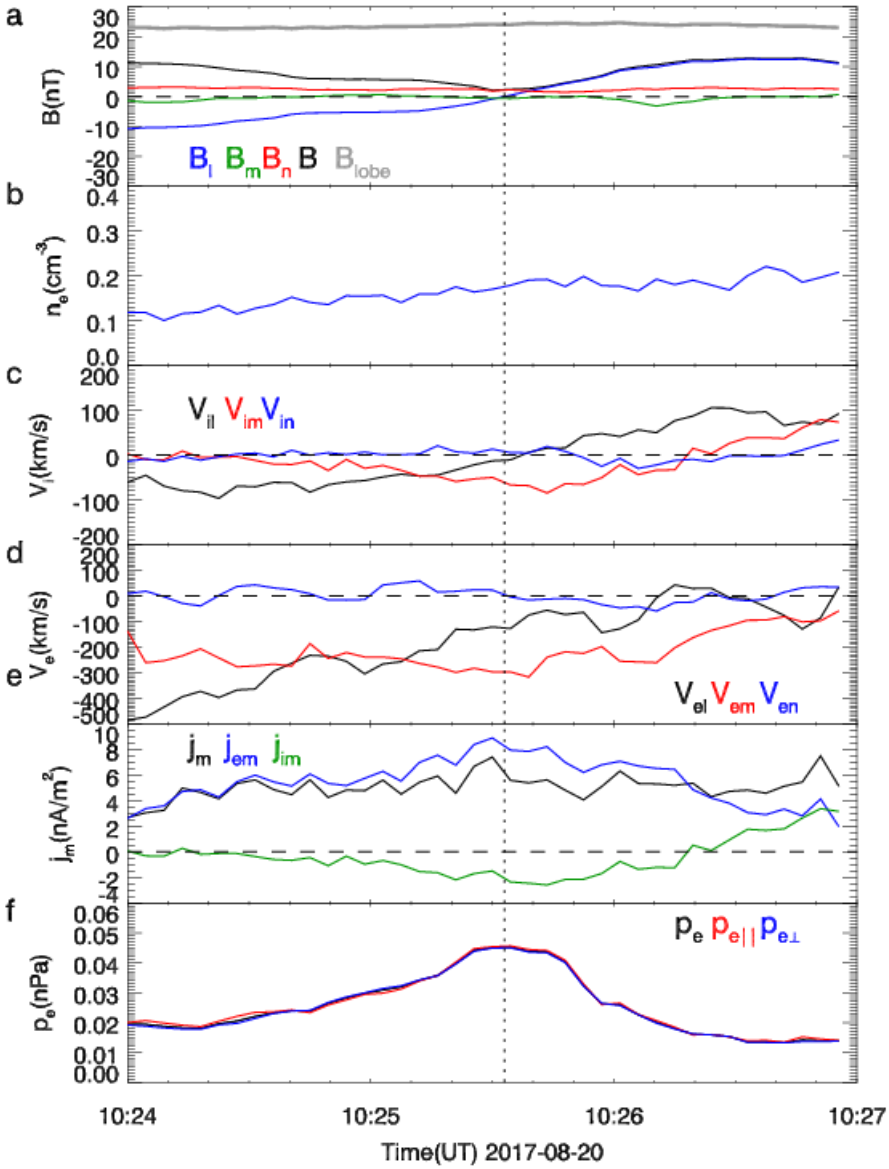

Figure 4. MMS1 observations of a TCS from 10:24 UT to 10:27 UT on August 20, 2017. (a) Magnetic field, (b) electron density, (c) ion flow velocity, (d) electron flow velocity, (e) current density and electron and ion contributions in the **m** direction, (f) electron pressure (black), electron parallel pressure (red), and electron perpendicular pressure (blue).

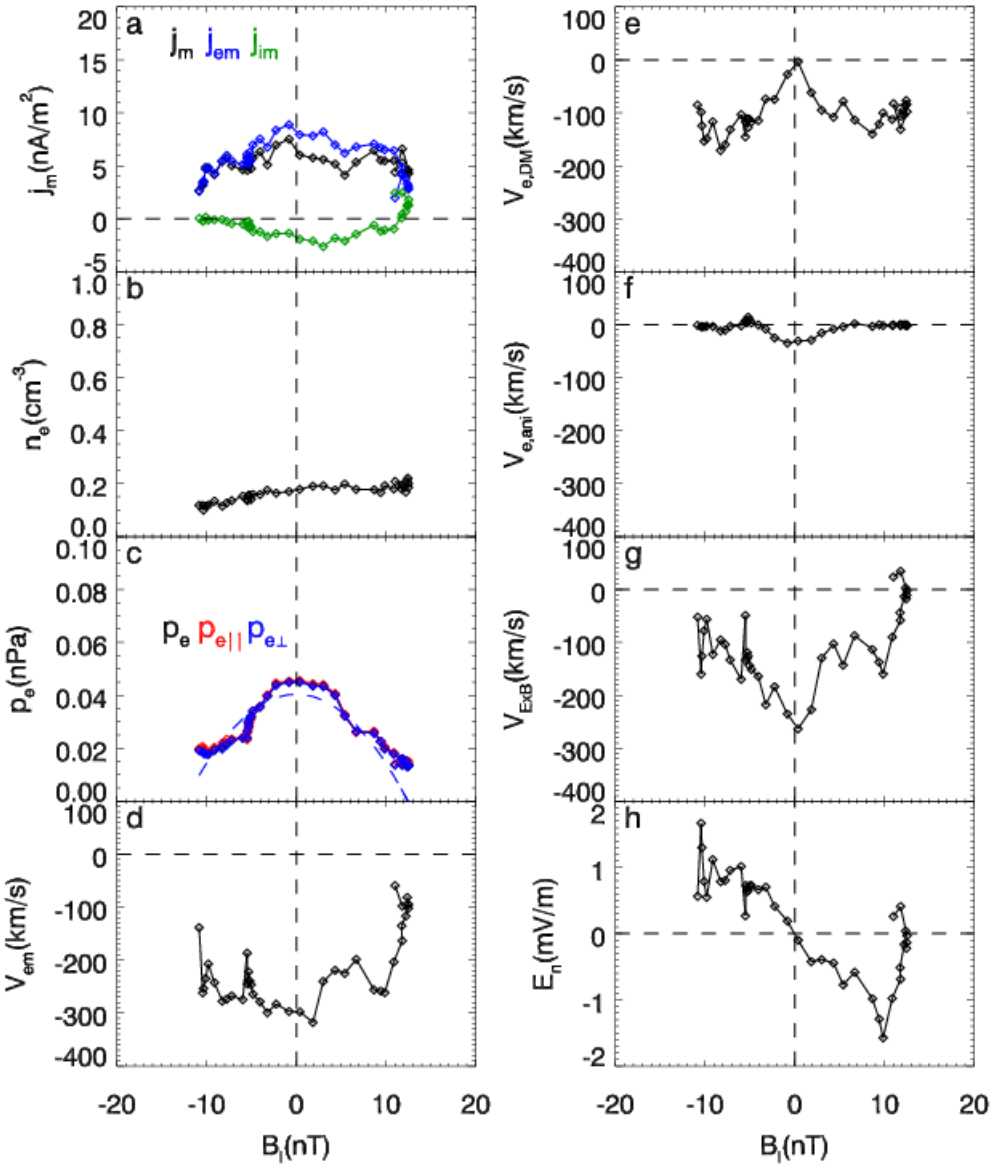

Figure 5. For the same event as shown in Figure 4. (a) Current density j_m (black), electron current density j_{em} (blue), and ion current density j_{im} (green); (b) electron density n_e; (c) electron pressure p_e (black), electron parallel pressure $p_{e\|}$ (red), and electron perpendicular pressure $p_{e\perp}$ (blue). The blue dashed curve represents the fitting of $p_{e\perp}$ using $p_{e\perp} = \hat{p}_{e\perp}(1 - \alpha B_l^2)$. (d) Electron bulk velocity V_{em} from direct measurements; (e) electron diamagnetic drift velocity $V_{e,DM}$; (f) electron anisotropy drift velocity $V_{e,ani}$; (g) electron $\mathbf{E} \times \mathbf{B}$ drift velocity $V_{E\times B}$; and (h) the Hall electric field E_n as functions of B_l – proxy of the distance from the neutral sheet.

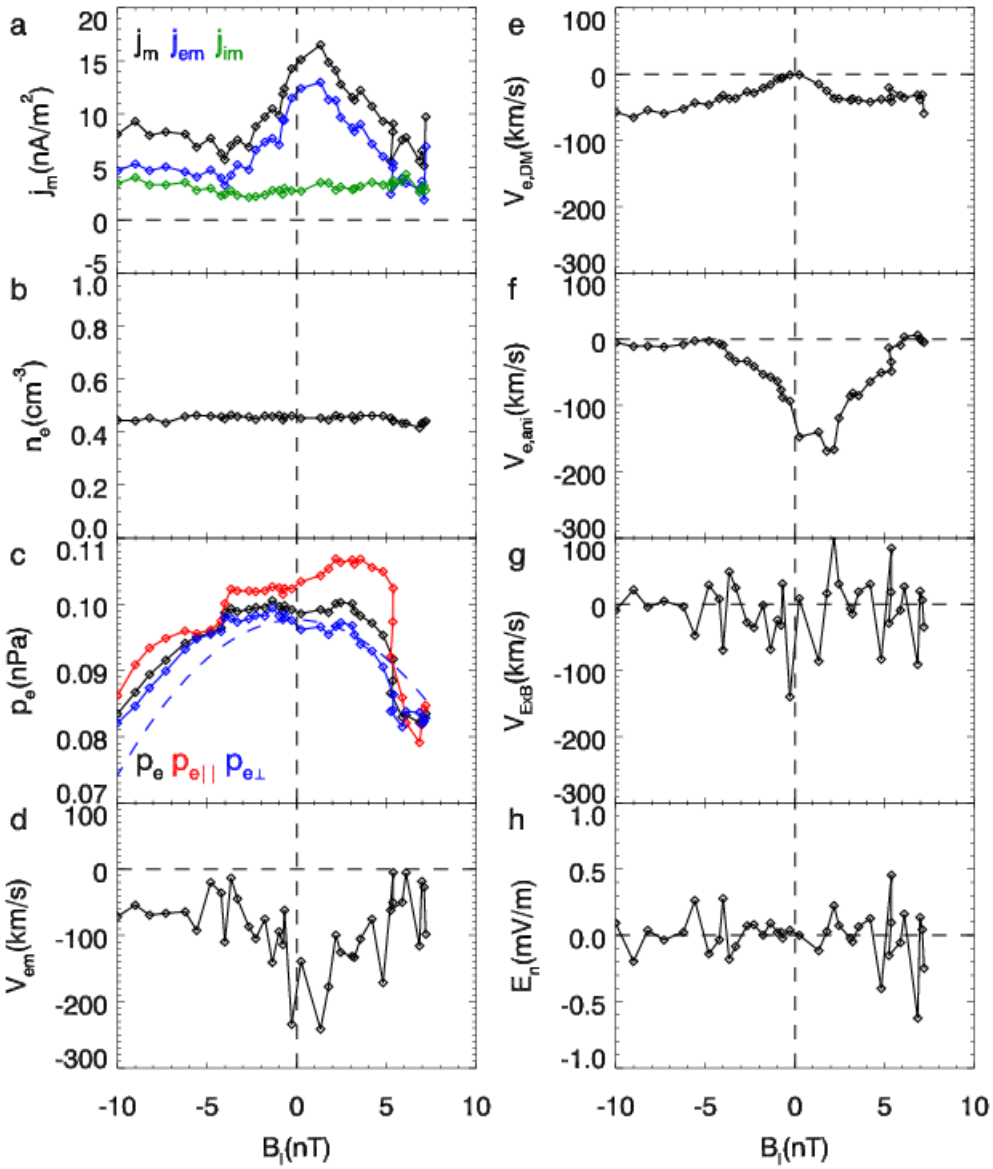

Figure 6. MMS1 observations of a TCS from 16:56 to 16:59 on August 18, 2017. Same format as Figure 5.

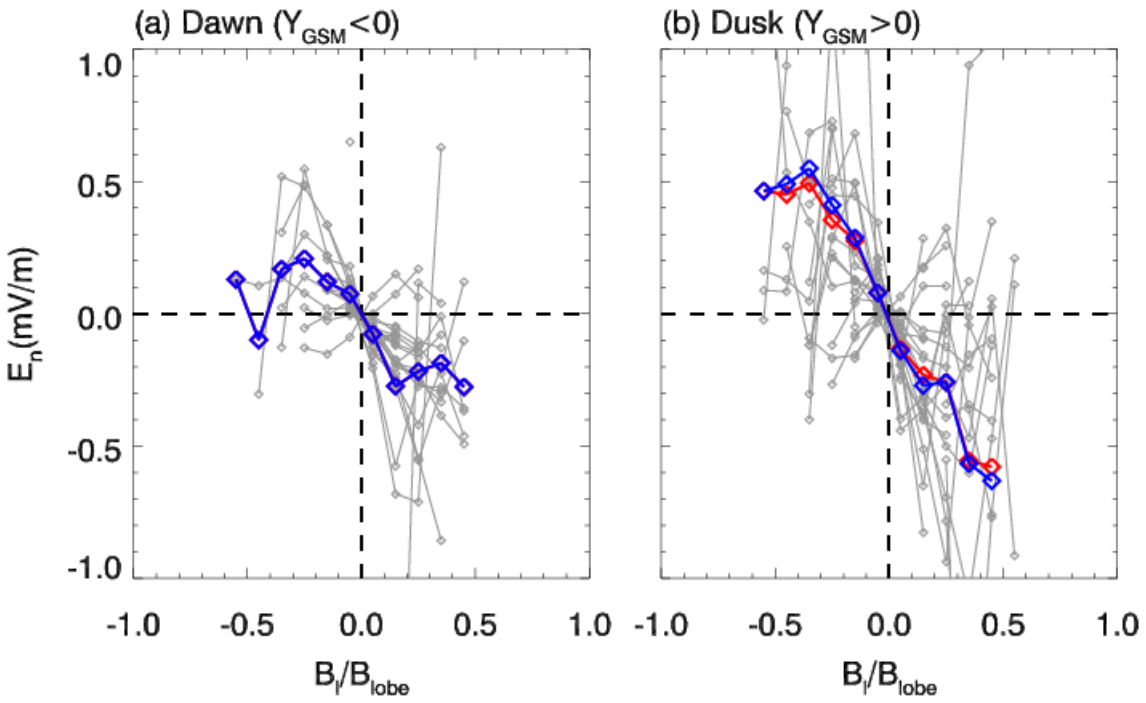

Figure 7. Statistics and dawn-dusk asymmetry from MMS measurements. The magnetic field B_l is normalized to the magnitude of the lobe magnetic field B_{lobe} (we use plasma pressure, $p_p = k_B(n_e T_e + n_i T_i)$ to calculate B_{lobe} from the current sheet pressure balance, $B_{lobe} = \left(B_x^2 + B_y^2 + 2\mu_0 p_p\right)^{1/2}$). Each gray curve represents a single event. The red curve denotes the average of all the events, and the blue curves denote the average of the events in which $\mathbf{E} \times \mathbf{B}$ drift dominates the electron velocity (i.e., the strong anisotropy events are excluded).

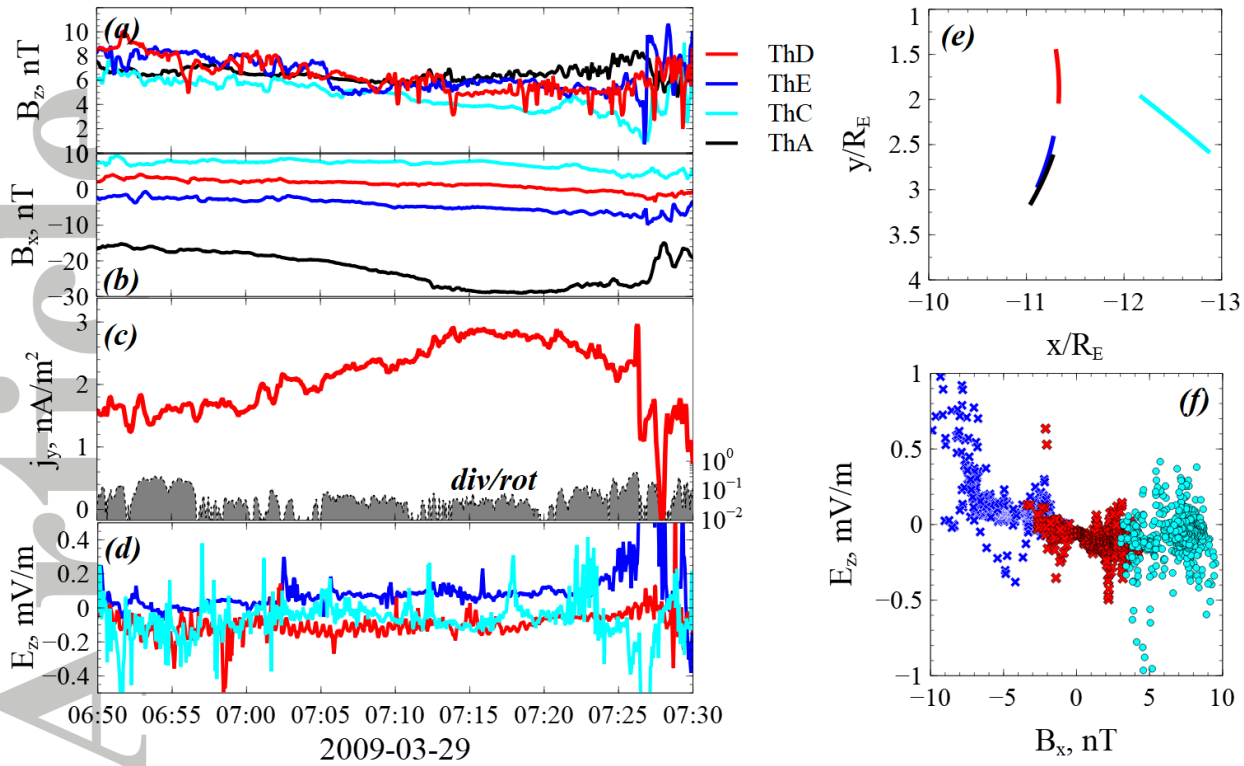

Figure 8. The current sheet thinning observed by four THEMIS spacecraft. Magnetic field components (a) B_z and (b) B_x, (c) current density j_y (and accuracy of the current density calculation), and (d) electric field E_z estimated from the $\mathbf{E} \cdot \mathbf{B} = 0$ approximation for three spacecraft. Panel (e) shows spacecraft locations in the GSM *x*-*y* plane, and panel (f) shows E_z distribution across the current sheet.

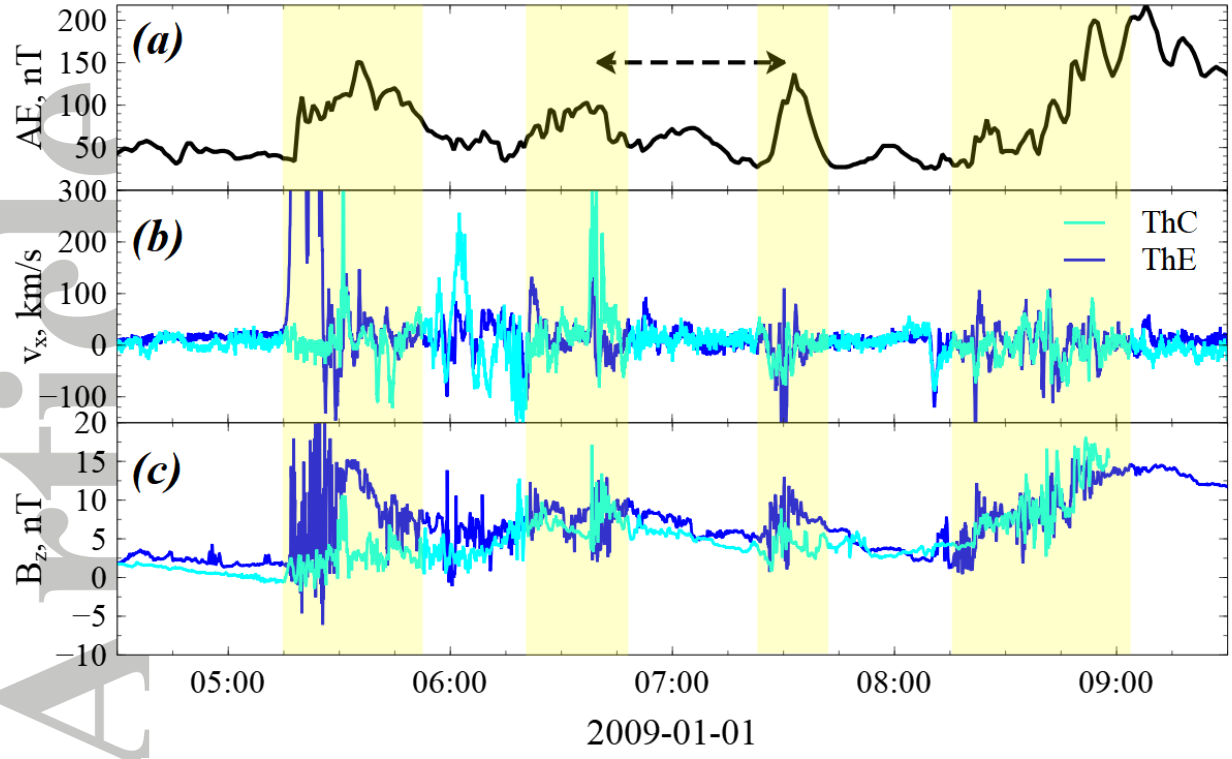

Figure 9. Long time interval that includes the subinterval of Figure 8 (indicated by the black arrow). (a) AE index, (b) plasma flow component V_x, and (c) magnetic field component B_z measured by THEMIS C and THEMIS E. The dipolarizations accompanied by fast plasma flows are shown by colored boxes.

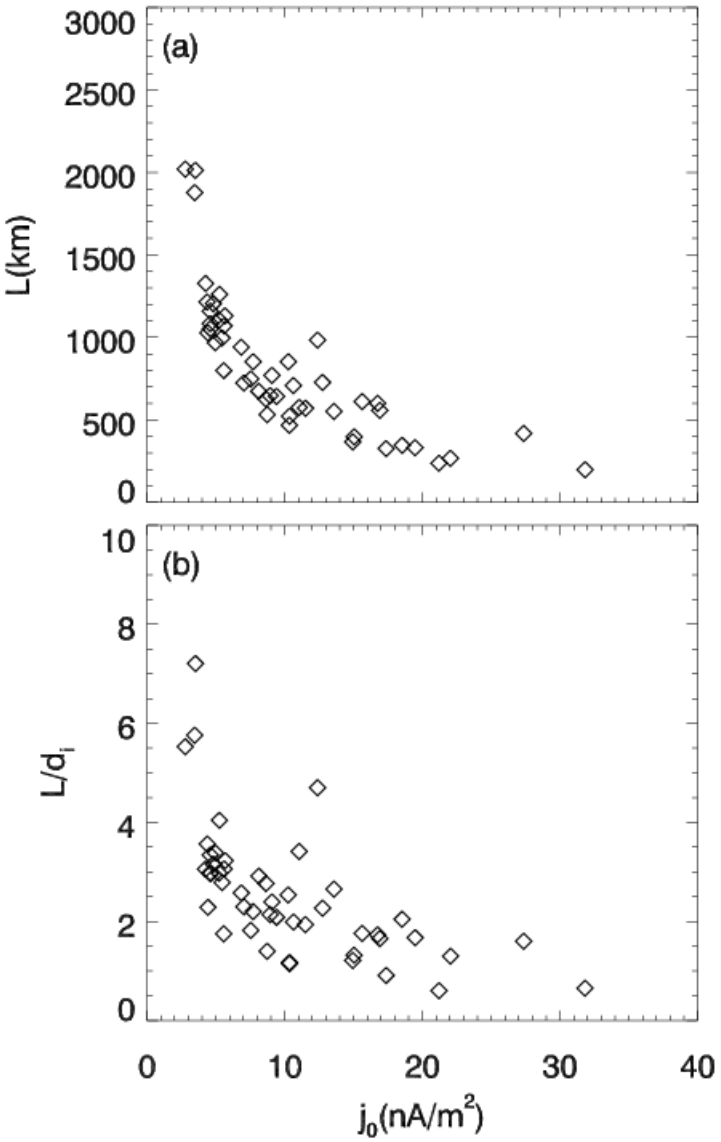

Figure A1. Current sheet thickness in the TCS events in units of (a) km and (b) local ion inertial length (d_i, evaluated using peak ion density).